

APPLIED SCIENCES AND ENGINEERING

Artificial tactile perception smart finger for material identification based on triboelectric sensing

Xuecheng Qu^{1†}, Zhuo Liu^{1,2†}, Puchuan Tan^{1,2†}, Chan Wang¹, Ying Liu^{1,3}, Hongqing Feng^{1,3}, Dan Luo^{1*}, Zhou Li^{1,3,4*}, Zhong Lin Wang^{1,3,5}

Tactile perception includes the direct response of tactile corpuscles to environmental stimuli and psychological parameters associated with brain recognition. To date, several artificial haptic-based sensing techniques can accurately measure physical stimuli. However, quantifying the psychological parameters of tactile perception to achieve texture and roughness identification remains challenging. Here, we developed a smart finger with surpassed human tactile perception, which enabled accurate identification of material type and roughness through the integration of triboelectric sensing and machine learning. In principle, as each material has different capabilities to gain or lose electrons, a unique triboelectric fingerprint output will be generated when the triboelectric sensor is in contact with the measured object. The construction of a triboelectric sensor array could further eliminate interference from the environment, and the accuracy rate of material identification was as high as 96.8%. The proposed smart finger provides the possibility to impart artificial tactile perception to manipulators or prosthetics.

INTRODUCTION

As an important sensory function for humans in direct contact with the external environment, tactile perception originates from the response of subcutaneous tactile corpuscles to different stimuli in the environment and the brain's recognition of signals afferent through nerve fibers. Therefore, the sense of touch not only reflects the tactile response to external physical stimuli (e.g., temperature, humidity, and pressure) but also includes a series of psychological parameters based on extraction and analysis of information by the brain, such as recognition of texture and roughness through tactile sensation. Bionic tactile sensors have attracted a great deal of attention since the 1980s, and high expectations are placed on simulating the tactile function of human skin. With the rapid development of functional materials and micro-nano processing technology, tactile sensors with high flexibility, spatial resolution, and sensitivity have been developed. Up to now, various types of physical information, including pressure (1–7), humidity (8, 9), and temperature (2, 7, 10), have been successfully identified through the contact of various sensing elements with objects based on piezoresistive (1, 2), capacitive (1), pyroelectric (10), and piezoelectric principles (11–14), which have been used in intelligent robots, medical rehabilitation, etc. (15–20). However, as psychosensory parameters are difficult to quantify, it remains challenging to simulate human tactile perception to determine the type and roughness of materials, which is crucial for the interaction between intelligent robots and the environment, in the context of both industrial sorting and the daily life of physically challenged people who rely on prosthetics.

Many efforts have been made to develop sensors or devices capable of identifying materials based on various strategies, such as thermal conductivity, ultrasound, computer vision, etc. (10, 21–26). As summarized in table S1, despite great progress in material recognition technology, it also has limitations. For example, identifying the material type by thermal conductivity has the advantages of low cost and high accuracy, but it requires long test times. Electromagnetic methods have good response speeds, but identification is limited to metals. Although computer vision has good robustness with respect to external noise, the integration of acquisition modules and algorithms is more complicated, and the types of materials that can be identified are limited. Therefore, there is an urgent need for a low-cost, high-efficiency, and widely applicable technique for tactile-like material identification.

On the basis of the coupling of triboelectrification and electrostatic induction, triboelectric nanogenerators (TENGs), as proposed by Z.L.W., can convert mechanical energy into electrical signals and have been widely used as energy-harvesting and sensing devices (27), such as biosensors (28, 29), implantable medical sensors (30–32), ocean energy-harvesting devices (33, 34), and biomechanical energy-harvesting devices (35–37), among other applications (38–47). The triboelectric effect refers to the contact-induced electrification that occurs at various interfaces. The transformation process from physical contact to electricity prompted us to use TENGs as a powerful tool for tactile perception simulation. Materials differ in their ability to gain and lose electrons, and surface electron transfer occurs when two materials come into contact; thus, materials take opposite charges after physical contact (40). According to the above theory, a triboelectric series can be established in which the unique position of each material determines the capacity and efficiency of charge exchange. Therefore, the fixed detector can effectively identify the type of touched material according to different triboelectric output signals.

In light of these considerations, we designed a triboelectric smart finger that surpassed human tactile perception for use in intelligent robots or artificial prosthetics (Fig. 1A). A sensor array composed of several typical materials in different positions in the triboelectric series was integrated into the smart finger, which could identify the

¹CAS Center for Excellence in Nanoscience, Beijing Key Laboratory of Micro-nano Energy and Sensor, Beijing Institute of Nanoenergy and Nanosystems, Chinese Academy of Sciences, Beijing 101400, China. ²Key Laboratory of Biomechanics and Mechanobiology, Ministry of Education, Beijing Advanced Innovation Center for Biomedical Engineering, School of Biological Science and Medical Engineering, Beihang University, Beijing 100191, China. ³School of Nanoscience and Technology, University of Chinese Academy of Sciences, Beijing 100049, China. ⁴Center of Nanoenergy Research, School of Physical Science and Technology, Guangxi University, Nanning 530004, China. ⁵School of Materials Science and Engineering, Georgia Institute of Technology, Atlanta, GA 30332-0245, USA.

*Corresponding author. Email: luodan@binn.cas.cn (D.L.); zli@binn.cas.cn (Z.Li)

†These authors contributed equally to this work.

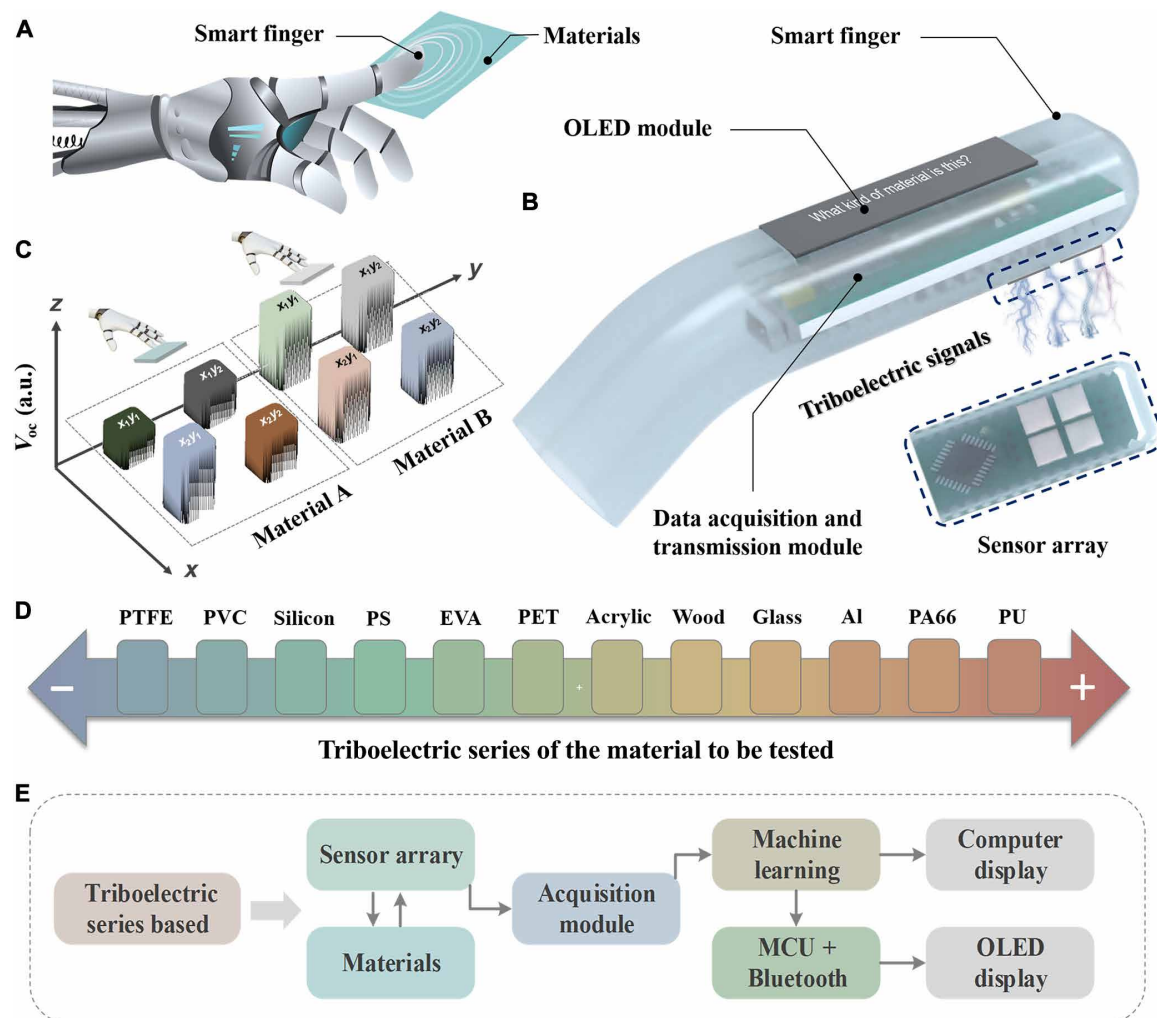


Fig. 1. Design and structure of the smart finger. (A) Schematic diagram of the material identification process of the triboelectric tactile perception smart finger. (B) Structure of the triboelectric tactile perception smart finger, consisting of a triboelectric sensor array, data acquisition and transmission module, and display module. (C) Schematic diagram of the output signals of the triboelectric sensor array when the smart finger identifies different materials. a.u., arbitrary units. (D) Typical materials located in different positions in the triboelectric series: Electronegativity increases from right to left; conversely, electropositivity increases from left to right. (E) Flowchart of the interaction between the modules of the smart finger when identifying materials.

type and roughness of materials based on triboelectric sensing. Moreover, machine learning–based data processing minimized environmental interference, substantially improving the identification accuracy to 96.8%. In addition, the wireless communication and display module integrated in the smart finger allowed the recognition results to be presented more intuitively. When the smart finger touched the material to be tested, the recognition information was directly projected onto the organic light-emitting diode (OLED) screen. This work quantified tactile psychological parameters through the triboelectric effect, which paves the way for a new era in modeling human tactile perception.

RESULTS

Design and integration of the triboelectric tactile perception smart finger

The triboelectric tactile perception smart finger was composed of a triboelectric sensor array, data acquisition and transmission module,

and display module (OLED screen), as shown in Fig. 1B. The triboelectric sensor array contained several discrete sensors, the signals from which reflected the characteristic information of the triboelectricity between the sensor and material in contact (Fig. 1C). Representative materials occupying different positions in the triboelectric series, such as polyamide (PA66), polyethylene terephthalate (PET), polystyrene (PS), and polytetrafluoroethylene (PTFE), were used as the friction layer for each sensor (Fig. 1D). Aluminum (Al) film was used as an electrode layer, constituting a single-electrode vertical contact separation mode triboelectric sensor. The portfolio of sensors with differentiated triboelectric properties ensured a distinct fingerprint output signal upon contact with a variety of materials, i.e., when the sensor contacted and separated from the test material, a unique voltage signal will be generated regardless of relative amplitude, voltage direction, or waveform. The acquisition module recorded these signals and then transmitted them to the computer through Bluetooth for machine learning. The recognition results were displayed on the computer screen through software or

on the OLED screen of the finger after Bluetooth transmission and microprogrammed control unit (MCU) processing (Fig. 1E).

Mechanism and operating parameters of the triboelectric sensor

In theory, triboelectric sensing is suitable for detecting all types of material. Contact electrification, the scientific term for triboelectricity, is a fundamental phenomenon that exists in various contact interfaces and can be explained by the overlapping electron cloud model. As shown in Fig. 2A, before the two materials come into contact on the atomic scale, their respective electron clouds are independent, without any overlapping regions. The potential well binds electrons tightly to specific orbitals, and no electron transfer occurs. When two atoms are in close contact, their electron clouds

overlap to form a bond. If an external force (such as pressure or friction) is applied, the bond length will be shortened, giving rise to a transition from initial single-well potential to asymmetric double-well potential. The strong electron cloud overlap weakens the energy barrier between atoms, allowing electrons to transfer from one atom to another (48). As the electron cloud states vary among different materials, the triboelectric signal between two given materials is unique. On the basis of the contact electrification theory, Wang further expanded the expression of displacement current in Maxwell's equation by introducing the $\frac{\partial P_s}{\partial t}$ term to describe the basic theory of nanogenerators, where P_s is the polarization density introduced by surface electrostatic charges caused by contact electrification or the piezoelectric effect (49)

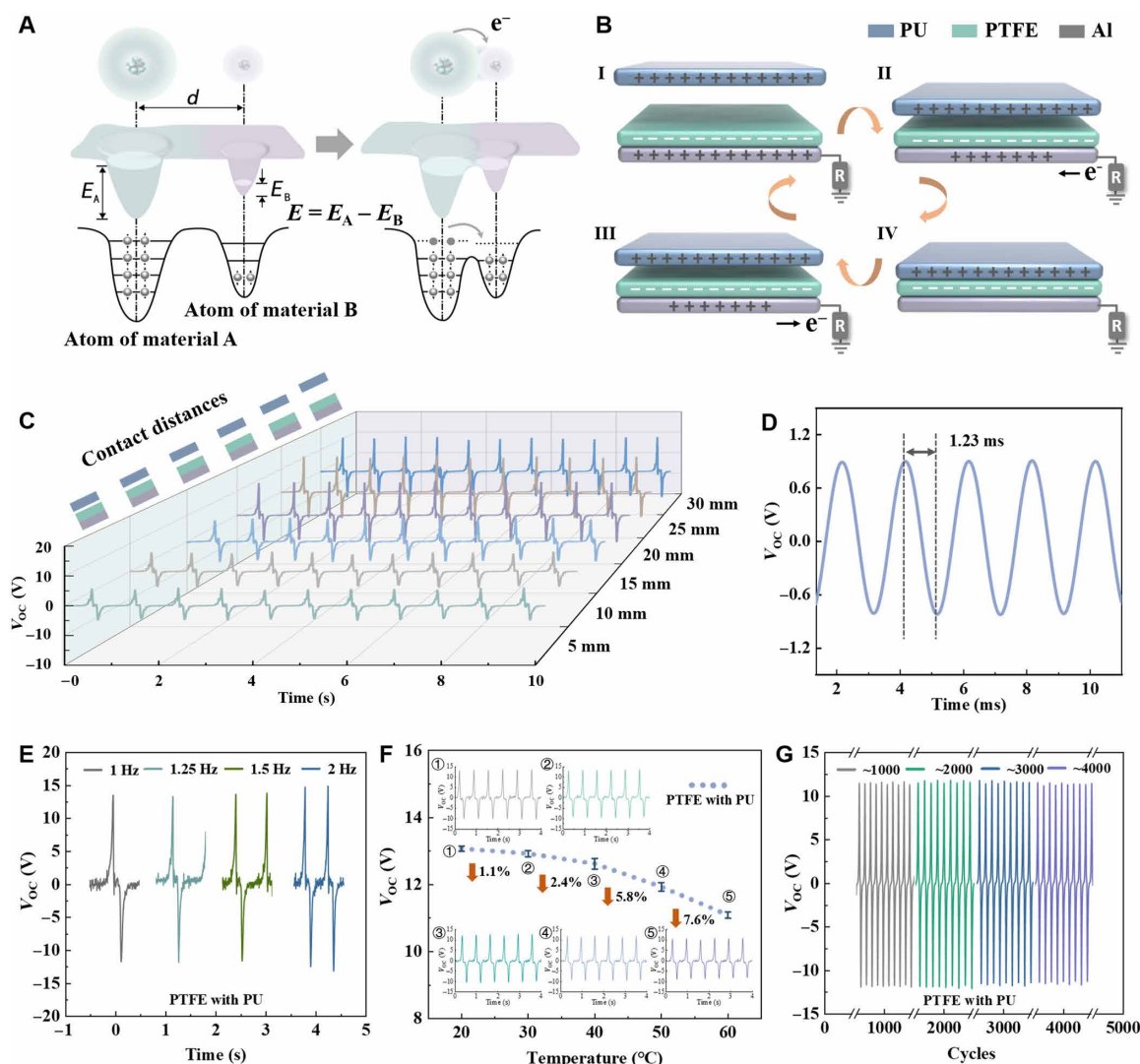


Fig. 2. Mechanism of triboelectric sensing and sensor performance characterization. (A) The fundamental principle of triboelectricity (also known as contact electrification) explained by the overlapping electron cloud model. (B) Working mechanism of triboelectric sensing based on a single-electrode vertical contact separation mode TENG. Example use of the triboelectric sensor with PTFE as a friction layer to identify PU. (C) V_{OC} at different contact distances between the triboelectric sensors (PTFE) and test material (PU). (D) Response time of the PTFE triboelectric sensor. (E) Influence of contact and separation frequency between the triboelectric sensor and measured material on V_{OC} . (F) V_{OC} output of the PTFE triboelectric sensor at different operating temperatures. (G) Fatigue testing of triboelectric sensing based on the model of PU detection by the PTFE triboelectric sensor.

$$\epsilon \nabla \cdot E = \rho - \nabla \cdot P_s \quad (1)$$

$$\nabla \cdot B = 0 \quad (2)$$

$$\nabla \times E = -\frac{\partial B}{\partial t} \quad (3)$$

$$\nabla \times H = J' + \epsilon \frac{\partial E}{\partial t} + \frac{\partial P_s}{\partial t} \quad (4)$$

$$J_D = \frac{\partial D}{\partial t} = \epsilon \frac{\partial E}{\partial t} + \frac{\partial P_s}{\partial t} \quad (5)$$

Note that E is the electric field, B stands for magnetic induction, H is the magnetic field intensity, ρ is the distribution of free charges in space, J is the density of free conduction current density in space as a result of charge flow, t is time, and D is the electric displacement vector. As the theoretical origin of the TENG, the addition of the P_s term to the electric displacement vector allows the application of Maxwell's equation in the fields of energy and sensing.

To illustrate the working principle of the triboelectric sensor, a sensor with PTFE as the friction layer was chosen as the research model, and the electropositive material, polyurethane (PU), was used as the test object. The operating mechanism of the sensor is shown schematically in Fig. 2B, which, in principle, involves the combination of triboelectrification and electrostatic induction and could be divided into four steps: (i) In the initial state, as the PU was far away from the triboelectric sensor, both the sensor side and measured object side were charge-balanced without generating any output signals; (ii) when the PU approached the sensor, the positive charges induced on the Al electrode decreased, and the electrons flowed from the reference electrode to the Al electrode; (iii) the potential difference between the Al electrode and PTFE reached a maximum value when the PU was in full contact with the triboelectric sensor; (iv) subsequently, the sensor was gradually separated from the PU test object. As the separation distance between the PU and sensor increased, the negatively charged PTFE induced more positive charges in the Al, driving the flow of free electrons from the Al electrode to the reference electrode, accompanied by the generation of a reverse output signal. The charges on both sides were rebalanced until the PU was completely separated from the PTFE. This constitutes a full cycle based on triboelectric sensing.

The corresponding relationships between the operating parameters of the sensor and its triboelectric output performance were systematically studied on the basis of the recognition of the PU model by the PTFE triboelectric sensor. As the primary factor under consideration, sensor size directly determined the strength of the output signal. Expectedly, the open circuit voltage (V_{OC}), short circuit current (I_{SC}), and transferred charge (Q_{SC}) were strongly positively correlated with the sensor size (fig. S1). In addition, the contact/separation distance also affected the triboelectric signal. Within a range of 5 to 20 mm, the V_{OC} gradually increased as the sensor moved away from the surface of the measured object, while it had little effect on V_{OC} when the distance exceeded 20 mm (Fig. 2C). The triboelectric sensor had a fast response speed of 1.23 ms, ensuring accurate material identification even with brief contact (Fig. 2D). Therefore, the normal contact and separation frequency between the sensor and material had little effect on the V_{OC} (Fig. 2E). Although the triboelectric sensing signal was temperature sensitive and the V_{OC} showed a

downward trend with increasing temperature (Fig. 2F), the detection signal was almost stable at room temperature (ranging from 20° to 30°C) with only 1.1% output attenuation. The triboelectric sensor retained high detection stability after repeated use under conventional environmental conditions (298 K, 1 atm). After 4000 cycles of testing, the output performance of the sensor showed no obvious attenuation or marked changes (Fig. 2G). Together, these observations showed that triboelectric sensing has the advantages of a simple structure, high applicability, good stability, and a fast response speed, making it ideal for simulating tactile perception.

Triboelectric fingerprint signal characteristics of different materials and surface roughnesses

On the basis of the working mechanism of the triboelectric sensor outlined above, a 2×2 triboelectric sensor array of PTFE, together with three other materials (PA66, PET, and PS), was constructed (Fig. 3A). According to the triboelectric series, PTFE has the strongest electronegativity among the four materials, followed by PS and PET, while PA66 is the most electropositive (electronegativity: PTFE > PS > PET > PA66). The combination of different sensors allowed more comprehensive feature information of the measured objects to be obtained, thereby effectively improving recognition accuracy.

To investigate the ability of triboelectric sensor arrays to discriminate between different material types even when the physical properties of the test object and sensor are similar, the same four materials used in sensors (PA66, PET, PS, and PTFE) were used as the test objects, and their output characteristics were studied separately. Identification of PTFE by the sensor array was investigated first. When the 2×2 triboelectric sensor array was in contact with and detached from the PTFE substrate, PET-, PS-, and PA66-based sensing units all produced similar “dip to peak” V_{OC} waveforms, due to the higher electronegativity of PTFE than PET, PS, and PA66 (Fig. 3B). Notably, the amplitude of the triboelectric output differed among the sensors, which was attributed to the difference among materials in the ability to gain and lose electrons. As shown in Fig. 3C, PA66 had a stronger tendency to lose electrons compared to PTFE; therefore, the PA66 sensor had the largest triboelectric output amplitude, followed by the PET and PS sensors. As PTFE was used as both the sensor and measured object, with the same ability to gain and lose electrons, the output amplitude of the PTFE sensor was the smallest. When PS was used as the test object, the V_{OC} waveforms output by the PET and PA66 sensors (dip to peak) were in the opposite direction to that of the PTFE sensor (peak to dip), because PS is weaker than PTFE but stronger than PET and PA66 in the electronegativity. Similarly, the material characteristic information reflected by the relative amplitude was also consistent with the difference in triboelectric series between materials (Fig. 3, D and E). Figure 3 (F and G) shows the V_{OC} waveform and relative amplitude when the sensor array detected PET, where the PA66 sensor had an inverted output signal waveform (dip to peak) compared to the PS and PTFE sensors (peak to dip). Compared to PTFE, PA66 had stronger electropositivity. When the sensor array detected PA66, the V_{OC} waveform and relative amplitude results were diametrically opposite to those obtained when identifying PTFE (Fig. 3, H and I). The applicability of the sensor array could be further extended to the identification of commonly used materials in daily life, including acrylic, ethylene-vinyl acetate copolymer (EVA), polyvinyl chloride (PVC), glass, PU, silicon, and wood. As shown in Fig. 3J and figs. S2 to S8,

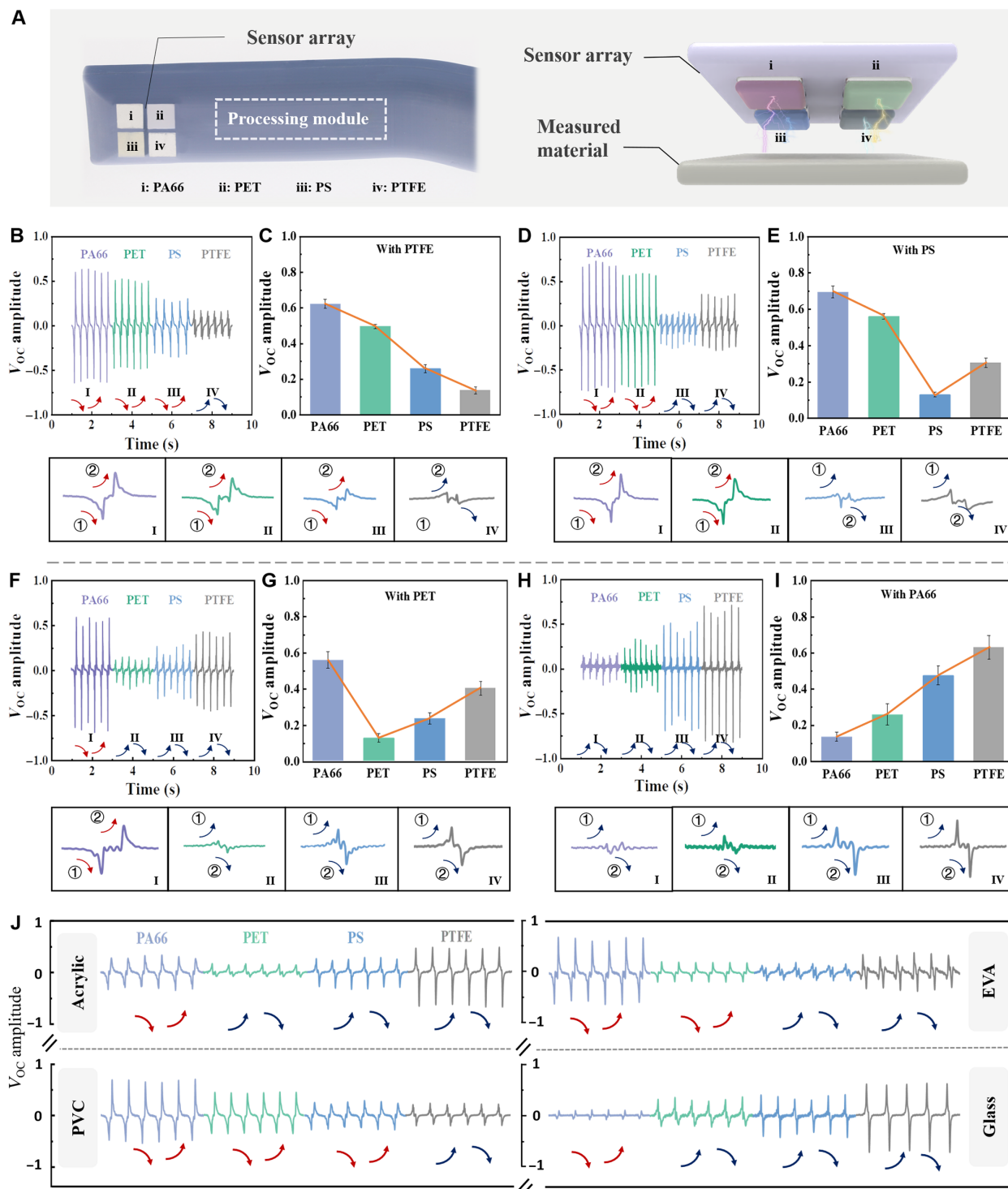


Fig. 3. Material type identification via the triboelectric sensor array. (A) Schematic diagram of the triboelectric sensor array on a smart finger. (B to I) The V_{oc} waveforms and amplitudes output when the sensor array (consisting of PA66, PET, PS, and PTFE triboelectric sensors) identified PTFE, PS, PET, and PA66, respectively. Top left: Output of each triboelectric sensor as it identified the material. Top right: Average amplitude of each triboelectric sensor output. Bottom: Amplified V_{oc} output of each triboelectric sensor. (J) V_{oc} output of the triboelectric sensor array when it detected acrylic, EVA, PVC, and glass, respectively.

the sensor array produced different triboelectric outputs upon contact/separation with each material, with unique waveform and relative amplitude characteristics. Moreover, the construction of the sensor array facilitated to eliminate interference by humidity with the electrical output. Humidity greatly affected the V_{OC} , as water has a certain electrical conductivity. In the sensor array, the relative voltage amplitude of the output signal of each sensor was barely disturbed by humidity, ensuring accurate identification of materials (fig. S9). These results confirmed the rationality of inferring the type of test material based on the triboelectric output characteristics.

In addition to distinguishing material types, the sensor array can also measure the roughness of each material (Fig. 4A). Four Al samples with different standard roughnesses ($R_a = 6.3, 3.2, 1.6$, and 0.8) were selected for analysis (photographs and micrographs of Al with four different roughnesses are shown in Fig. 4B and fig. S10). The roughness reflects the microtopological features of the material surface consisting of peaks and dips, where a smaller R_a value represents closer peak spacing. During measurement, the sensor array was grounded as a reference, which effectively prevented the accumulation of frictional charges and reduced external interference. The average distance between adjacent grooves for samples with R_a values of 6.3, 3.2, 1.6, and 0.8 are about 1.4, 1.0, 0.8, and 0.5 mm,

respectively. As the roughness decreased, the V_{OC} generated by the sensor array increased, which was attributed to the denser microstructure increasing the interface area between the sample and sensor array, enabling it to induce and accumulate more charge. It is worth noting that the increase in V_{OC} caused by roughness would not be erroneously identified as a different material type. Although the absolute V_{OC} values for the Al samples with four roughnesses were different, the electrical signals output by each sensor in the sensor array maintained a consistent relative ratio, indicating that the sensor array was detecting the same material (Fig. 4C and fig. S11).

The traditional contact stitch roughness detection methods cause great abrasions of the equipment and samples, and errors are likely to occur after multiple measurements. In contrast, fatigue testing confirmed that the performance of the triboelectric sensor array was almost unchanged after multiple uses, fully demonstrating the advantages of triboelectric sensing in contact/separation mode with regard to wear suppression (fig. S12). Compared to commercial probe-based roughness analysis strategies, triboelectric sensing is more convenient and economical and does not damage the sample surface; thus, it can be used for roughness detection in fine industrial manufacturing.

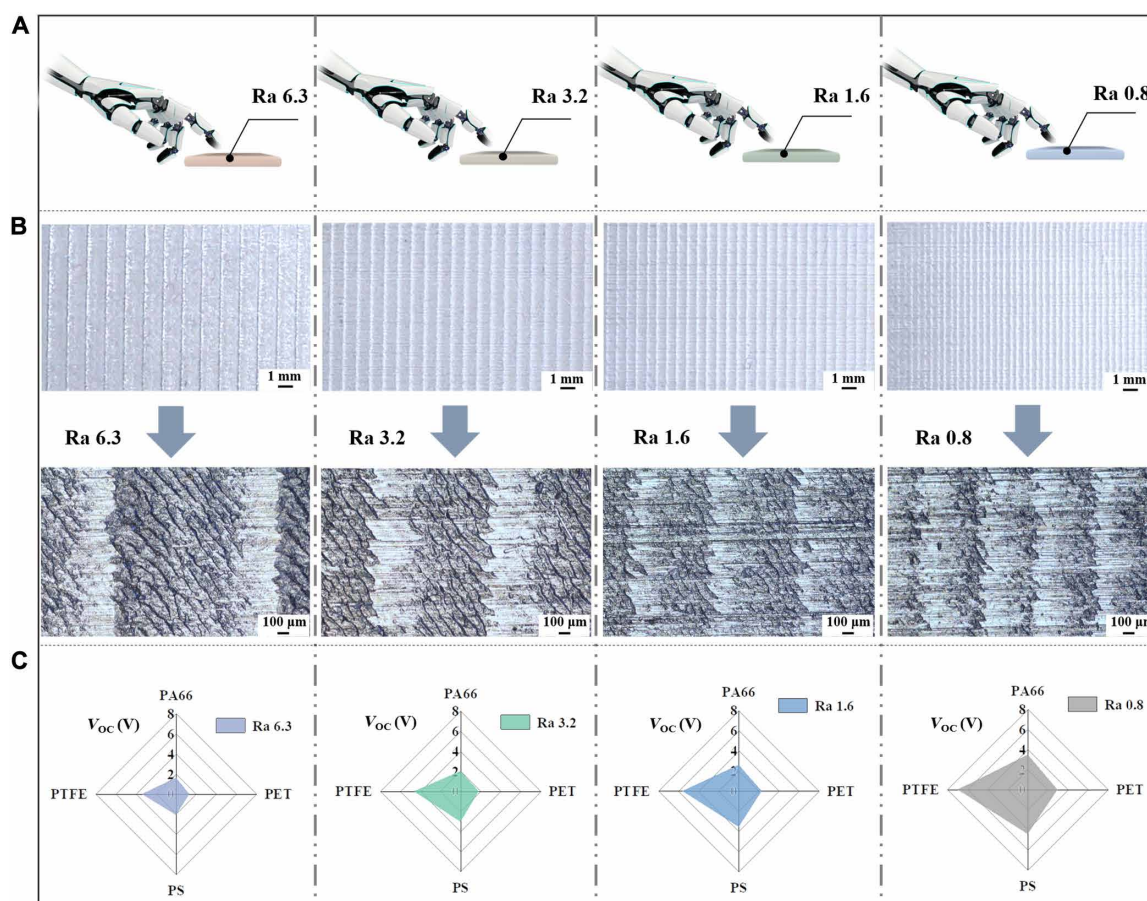


Fig. 4. Identification of material roughness by the triboelectric sensor array. (A) Schematic diagram of aluminum roughness detection by the triboelectric tactile perception smart finger. (B) Photographs (top) and micrographs (bottom) of aluminum with different roughnesses. (C) The V_{OC} of the triboelectric sensor array when identifying Al with different roughnesses. When the triboelectric sensor array identified samples with different roughness but the same texture, the triboelectric output signals of the four sensors expanded proportionally, thus preventing misidentification as other materials.

Integrating machine learning enables material recognition accuracy up to 96.8%

Machine learning has been shown to be an effective tool for automatically extracting features from the time-domain data of triboelectric signals and for high-precision identification of different samples (50). On the basis of the processing of these signals, differences between materials are amplified and clearly presented. However, direct learning of time series data will lead to an excessive data volume and huge costs in terms of both calculation time and memory space. Therefore, feature extraction is a prerequisite for machine learning (51). Here, multiple features of the data were learned, and features with the greatest impact on prediction accuracy for machine learning including the maximum value, minimum-maximum, peak-valley interval, number of zero-crossing points, number of inflection points, and absolute square value were lastly selected. Figure 5A presents a flowchart showing the details of the material identification using the smart finger with the assist of machine learning. Initially, the collected data of known materials were preprocessed.

After feature extraction and selection, a machine learning model was established between the feature matrix and the labels and then iterated continuously. As the amount of training data increased, the machine learning model gradually approached the ground truth. The material category could be judged after the model was established. The entire material recognition system required a short response time, so the deep learning method with a long calculation time was abandoned, and the linear discriminant analysis (LDA) algorithm, a supervised learning dimensionality reduction technique in machine learning, was chosen. With the LDA algorithm, high-dimensional data for visualization in low-dimensional space (two dimensions) were successfully used, with the aim of minimizing the distances between the projection points of each data category while maximizing those between the centers of different data categories. As shown in Fig. 5B, when the original data were from a single channel, the clustering of samples was less ordered, and the machine learning classification accuracy rate was only 52.7%. As the number of channels (i.e., the number of sensors) increased, the clustering of samples

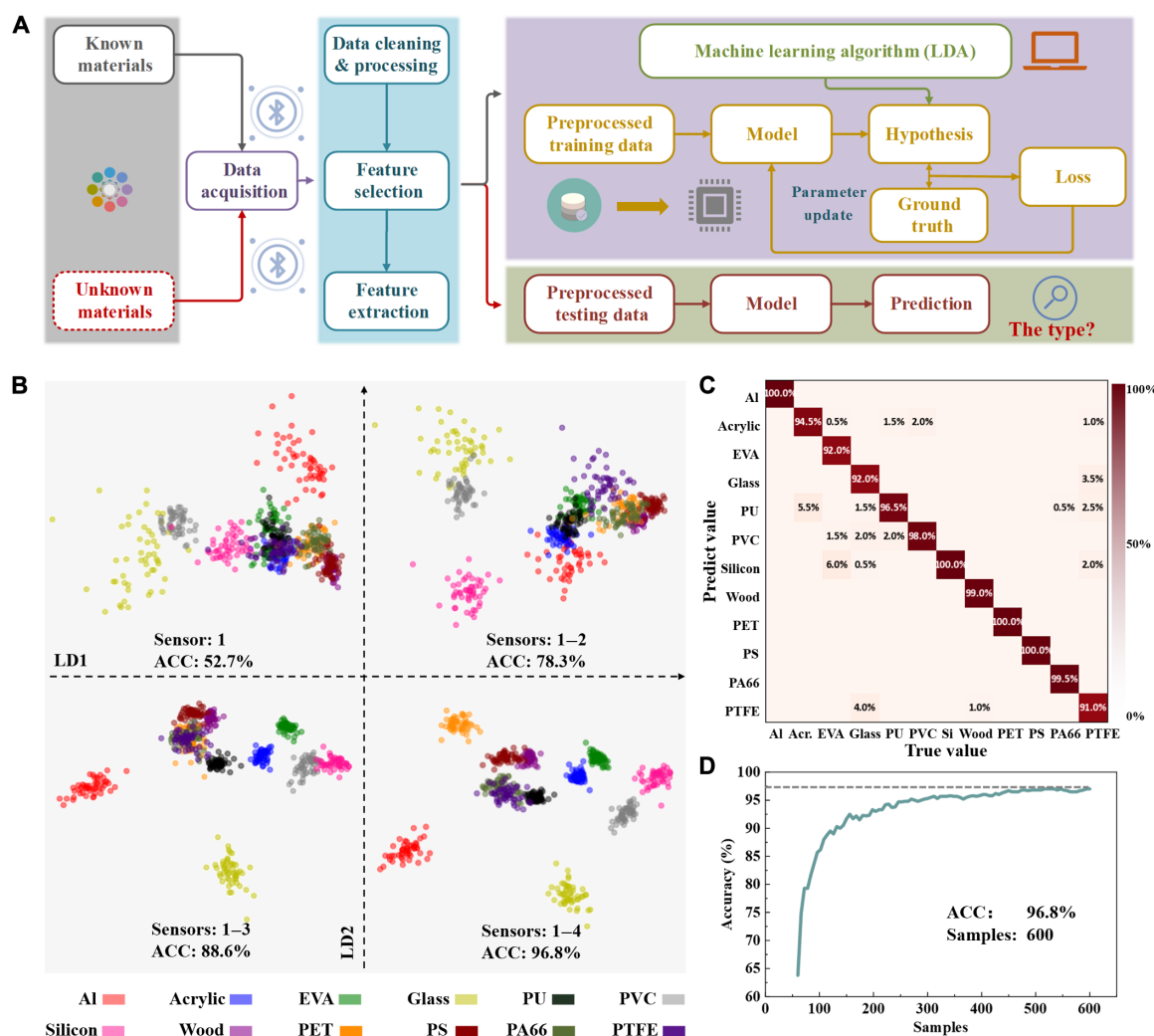


Fig. 5. Machine learning–based data processing for high-accuracy material type identification. (A) Flow diagram of machine learning for material identification. (B) Prediction accuracy for material types differing in channel numbers. (C) Confusion map of the machine learning results for 12 objects with four channels. (D) Prediction accuracy for different sample sizes. ACC, accuracy.

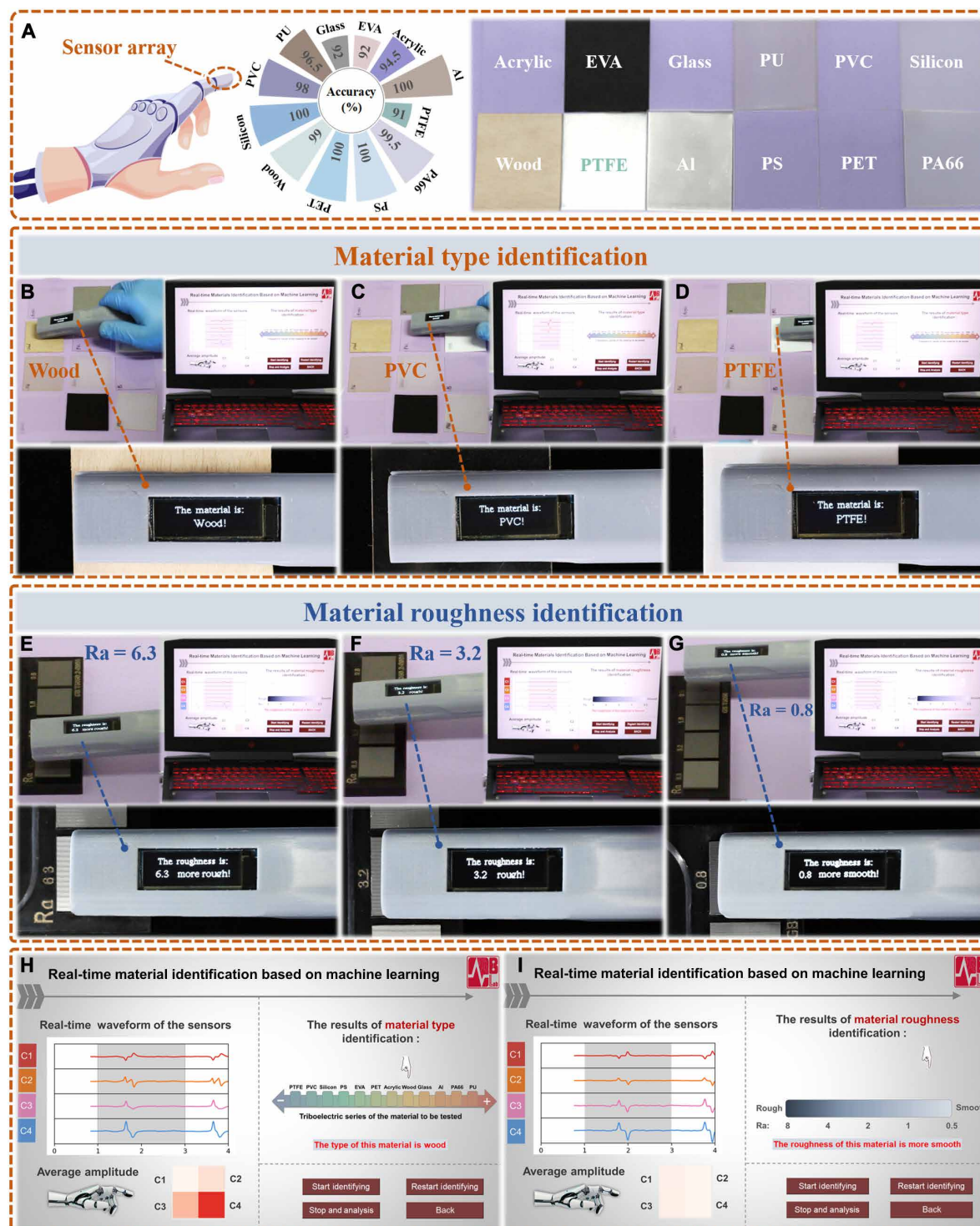


Fig. 6. Practical application scenarios of material type and roughness identification by the smart finger and the interactive interface. (A) Photographs of several test materials and the corresponding identification accuracy. (B to D) With the aid of machine learning, the smart finger successfully identified the material type, and the results were displayed on the OLED screen. (E to G) The roughness detection process used by the smart finger; the recognition results were displayed on the OLED screen. (H and I) The computer interface for material type and surface roughness identification.

became clearer. With data collection from four channels, several sample points of each object were clustered together to clearly classify the material type with an accuracy rate of up to 96.8%. The confusion matrix of 12 materials is shown in Fig. 5C, and high perceptual accuracy was achieved for all 12 materials. The number of samples also affected the accuracy of machine learning, which increased with increasing sample size (Fig. 5D). In addition, the prediction accuracy rate for material roughness can also reach up to 96.5%. The corresponding scatterplots and confusion matrix of test results are shown in fig. S13. The previous strategy strongly relied on increasing the quantity of sensors for a relatively accurate classification, which made data processing more complicated. With the application of machine learning, a good balance between the number of sensors and the accuracy of predictions made by the smart finger could be achieved. In this study, multiple materials could be recognized with a minimal number of triboelectric sensors; this should greatly reduce the difficulty and cost of equipment manufacturing while ensuring the accuracy of identification.

Triboelectric tactile perception smart finger intuitively and accurately identified the type and roughness of various common materials

To demonstrate the real-world feasibility of the integrated triboelectric sensing system for material type and roughness identification, a smart finger with transcended human tactile perception was constructed, which integrated a triboelectric sensor array, data acquisition and transmission module, and display module (fig. S14). The multichannel, high-precision acquisition module could accurately record signals containing detailed information on material characteristics. The signals were then transmitted to the computer via Bluetooth for machine learning, and the results were displayed on the computer monitor or OLED screen of the smart finger in real time after being transmitted to the built-in MCU via Bluetooth. The smart finger can be integrated into intelligent prostheses or manipulators and recognizes various textures such as polymers, metals, and wood. Several materials were selected as test objects, including acrylic, EVA, glass, PU, PVC, silicon, wood, PTFE, Al, PS, PET, and PA66; the recognition accuracies are shown in Fig. 6A.

During operation, when the smart finger continuously touched the material twice under suitable conditions (approximately 2 cm away from the object), machine learning was applied to the collected signals, and the final prediction results were intuitively displayed on the computer monitor or OLED screen of the smart finger (Fig. 6, B to D, and fig. S15). The computer terminal display interface for material type identification is shown in Fig. 6H and fig. S16. The left half of the software display interface shows the waveform and peak statistical information, collected in real time, and the right half shows the identification result (e.g., wood in Fig. 6H). The roughness recognition results are shown in Fig. 6 (E to G) and fig. S17. Similarly, Fig. 6I and fig. S18 show the display interface for material roughness analysis (Al, $R_a = 0.8$). The process of simulating tactile perception is shown in detail in movies S1 to S4.

DISCUSSION

Here, we proposed a strategy to simulate human tactile perception and quantify tactile psychosensory parameters based on triboelectric sensing. As the ability to gain and lose electrons differs among materials, triboelectric fingerprint outputs with unique amplitudes

and waveforms could be generated when the triboelectric sensor array was placed in contact with different objects. On the basis of the above principles, we developed a smart finger with transcended human tactile perception for use in prosthetics and manipulators to achieve identification of material type and roughness. With the aid of machine learning, the material recognition accuracy rate was as high as 96.8% under the premise of using only four sensors, and a variety of common materials (such as acrylic, EVA, glass, PU, PVC, silicon, and wood) could be recognized accurately. In addition, integration of the wireless transmission and display modules into the smart finger freed it from the requirement for a data cable, and the recognition results were displayed intuitively on the OLED screen.

The triboelectric tactile perception smart finger has the advantages of simple fabrication, a fast response, high accuracy, wide applicability, and sensing without damaging samples. Going forward, more complex and practical applications could be achieved by building interfaces of smart fingers with robots or even humans. For example, it could help robots to check whether products meet manufacturing standards in terms of composition and surface structure or help physically challenged people who rely on prosthetics to recreate their perception of the external environment. On the other hand, further research is required to improve the flexibility, miniaturization, and multifunctionalities of the sensors. In the future, artificial intelligence chips will be integrated into smart fingers to make them “smarter” and confer the ability to process data independent of the computer. In addition, pressure, temperature, and humidity sensors will be introduced to build a combination of multimodal information. It is believed that the tactile simulation technology based on triboelectric sensing has great potential in the fields of medical rehabilitation and intelligent industry.

MATERIALS AND METHODS

Fabrication of smart finger

The smart finger was integrated with a sensor array, signal acquisition module, processing module, communication module, and OLED screen. The sensor array was composed of four TENGs, each with high-purity materials: PA66, PET, PS, and PTFE film were used as the friction layer, and the Al foil was used as the friction layer attached on the surface of the high-purity materials, respectively. The size of each sensor is 1 cm by 1 cm. The case of the smart finger was printed by a three-dimensional printer. The sensor array was integrated under the fingertip, the acquisition module and the communication module were inside the cavity of the smart finger, and the OLED screen was fixed in the card slot above the finger. OpenBCI multichannel open-source module was used as the acquisition module, the analog front-end chip was Texas Instruments ADS1299 (high-gain, low-noise analog-to-digital converter (ADC), 24-bit channel resolution, and up to 16-kHz sampling rate), the main control chip was Arduino Uno (Atmel Atmega328P), and the communication was wireless (Bluetooth Low Energy) to realize wireless signal transmission. The machine learning part was completed on the computer side, using Python language.

Characterization and measurement

The output performance (open-circuit voltage, short-circuit current, and transferred charge) of the sensor was measured and recorded by an electrometer (6514, Keithley; 344-K, TRKE) and oscilloscope (HD 4096, Teledyne LeCroy). The basic data acquisition used a linear

motor (E1100, LinMot, 1-Hz frequency) to simulate the manipulator for contact and separation (contact distance, 20 mm; contact pressure, 5 N). In the fatigue test, the sensor was driven periodically by a linear motor (E1100, LinMot, 1-Hz frequency). The fatigue test was performed for 4000 cycles. In the response time test, the PU film was attached to the force-applying side of the vibrating table, and the sensor (with PTFE as the friction layer) was fixed on the top of the PU film with a shelf, leaving a 2-mm gap between the sensor and the PU film. Then, the sensor was driven periodically by a vibration table (VT-500, YMC Piezotronics, 400-Hz frequency, 2-mm motion amplitude). The photos were taken by a digital camera (Canon EOS, 6D Mark II). Micrographs were taken by an optical microscope (ECLIPSE LV100ND, Nikon). The negative electrodes of the test line were grounded during the test to reduce external interference. All data are obtained after multiple measurements. The ordinate amplitude data are normalized by mathematical transformation.

SUPPLEMENTARY MATERIALS

Supplementary material for this article is available at <https://science.org/doi/10.1126/sciadv.abq2521>

REFERENCES AND NOTES

1. L. Beker, N. Matsuhisa, I. You, S. R. A. Ruth, S. Niu, A. Foudeh, J. B. H. Tok, X. Chen, Z. Bao, A bioinspired stretchable membrane-based compliance sensor. *Proc. Natl. Acad. Sci. U.S.A.* **117**, 11314–11320 (2020).
2. J. Park, M. Kim, Y. Lee, H. S. Lee, H. Ko, Fingertip skin-inspired microstructured ferroelectric skins discriminate static/dynamic pressure and temperature stimuli. *Sci. Adv.* **1**, e1500661 (2015).
3. Z. Liu, Y. Ma, H. Ouyang, B. Shi, N. Li, D. Jiang, F. Xie, D. Qu, Y. Zou, Y. Huang, H. Li, C. Zhao, P. Tan, M. Yu, Y. Fan, H. Zhang, Z. L. Wang, Z. Li, Transcatheter self-powered ultrasensitive endocardial pressure sensor. *Adv. Funct. Mater.* **29**, 1807560 (2019).
4. X. Pu, H. Guo, J. Chen, X. Wang, Y. Xi, C. Hu, Z. L. Wang, Eye motion triggered self-powered mechnosensational communication system using triboelectric nanogenerator. *Sci. Adv.* **3**, e1700694 (2017).
5. C. Wang, X. Qu, Q. Zheng, Y. Liu, P. Tan, B. Shi, H. Ouyang, S. Chao, Y. Zou, C. Zhao, Z. Liu, Y. Li, Z. Li, Stretchable, self-healing, and skin-mounted active sensor for multipoint muscle function assessment. *ACS Nano* **15**, 10130–10140 (2021).
6. H. J. Yoon, D. M. Lee, Y. J. Kim, S. Jeon, J. H. Jung, S. S. Kwak, J. Kim, S. Kim, Y. Kim, S. W. Kim, Mechanoreceptor-inspired dynamic mechanical stimuli perception based on switchable ionic polarization. *Adv. Funct. Mater.* **31**, 2100649 (2021).
7. F. Zhang, Y. Zang, D. Huang, C. A. Di, D. Zhu, Flexible and self-powered temperature-pressure dual-parameter sensors using microstructure-frame-supported organic thermoelectric materials. *Nat. Commun.* **6**, 8356 (2015).
8. J. Yang, R. Shi, Z. Lou, R. Chai, K. Jiang, G. Shen, Flexible smart noncontact control systems with ultrasensitive humidity sensors. *Small* **15**, 1902801 (2019).
9. T. Li, L. Li, H. Sun, Y. Xu, X. Wang, H. Luo, Z. Liu, T. Zhang, Porous ionic membrane based flexible humidity sensor and its multifunctional applications. *Adv. Sci.* **4**, 1600404 (2017).
10. S. Zhao, R. Zhu, A smart artificial finger with multisensations of matter, temperature, and proximity. *Adv. Mater. Technol.* **3**, 1800056 (2018).
11. Z. Liu, Q. Zheng, Y. Shi, L. Xu, Y. Zou, D. Jiang, B. Shi, X. Qu, H. Li, H. Ouyang, R. Liu, Y. Wu, Y. Fan, Z. Li, Flexible and stretchable dual mode nanogenerator for rehabilitation monitoring and information interaction. *J. Mater. Chem. B* **8**, 3647–3654 (2020).
12. W. Guo, C. Tan, K. Shi, J. Li, X. X. Wang, B. Sun, X. Huang, Y. Z. Long, P. Jiang, Wireless piezoelectric devices based on electrospun PVDF/BaTiO₃ NW nanocomposite fibers for human motion monitoring. *Nanoscale* **10**, 17751–17760 (2018).
13. B.-Y. Lee, D. H. Kim, J. Park, K.-I. Park, K. J. Lee, C. K. Jeong, Modulation of surface physics and chemistry in triboelectric energy harvesting technologies. *Sci. Technol. Adv. Mater.* **20**, 758–773 (2019).
14. H. S. Wang, S. K. Hong, J. H. Han, Y. H. Jung, H. K. Jeong, T. H. Im, C. K. Jeong, B.-Y. Lee, G. Kim, C. D. Yoo, K. J. Lee, Biomimetic and flexible piezoelectric mobile acoustic sensors with multiresonant ultrathin structures for machine learning biometrics. *Sci. Adv.* **7**, eabe5683 (2021).
15. T. Chen, Q. Shi, M. Zhu, T. He, L. Sun, L. Yang, C. Lee, Triboelectric self-powered wearable flexible patch as 3D motion control interface for robotic manipulator. *ACS Nano* **12**, 11561–11571 (2018).
16. T. Jin, Z. Sun, L. Li, Q. Zhang, M. Zhu, Z. Zhang, G. Yuan, T. Chen, Y. Tian, X. Hou, C. Lee, Triboelectric nanogenerator sensors for soft robotics aiming at digital twin applications. *Nat. Commun.* **11**, 5381 (2020).
17. Z. Sun, M. Zhu, Z. Zhang, Z. Chen, Q. Shi, X. Shan, R. C. H. Yeow, C. Lee, Artificial intelligence of things (AIoT) enabled virtual shop applications using self-powered sensor enhanced soft robotic manipulator. *Adv. Sci.* **8**, e2100230 (2021).
18. J. Kim, M. Lee, H. J. Shim, R. Ghaffari, H. R. Cho, D. Son, Y. H. Jung, M. Soh, C. Choi, S. Jung, K. Chu, D. Jeon, S. T. Lee, J. H. Kim, S. H. Choi, T. Hyeon, D. H. Kim, Stretchable silicon nanoribbon electronics for skin prosthesis. *Nat. Commun.* **5**, 5747 (2014).
19. G. Lee, J. H. Son, S. Lee, S. W. Kim, D. Kim, N. N. Nguyen, S. G. Lee, K. Cho, Fingerpad-inspired multimodal electronic skin for material discrimination and texture recognition. *Adv. Sci.* **8**, 2002606 (2021).
20. S. Wang, J. Xu, W. Wang, G.-J. N. Wang, R. Rastak, F. Molina-Lopez, J. W. Chung, S. Niu, V. R. Feig, J. Lopez, T. Lei, S.-K. Kwon, Y. Kim, A. M. Foudeh, A. Ehrlich, A. Gasperini, Y. Yun, B. Murmann, J. B. H. Tok, Z. Bao, Skin electronics from scalable fabrication of an intrinsically stretchable transistor array. *Nature* **555**, 83–88 (2018).
21. H. S. Lee, J. Chung, G.-T. Hwang, C. K. Jeong, Y. Jung, J.-H. Kwak, H. Kang, M. Byun, W. D. Kim, S. Hur, S.-H. Oh, K. J. Lee, Flexible inorganic piezoelectric acoustic nanosensors for biomimetic artificial hair cells. *Adv. Funct. Mater.* **24**, 6914–6921 (2014).
22. M. K. Ramasubramanian, R. A. Venditti, C. Ammineni, V. Mallapragada, Optical sensor for noncontact measurement of lignin content in high-speed moving paper surfaces. *Ieee Sens. J.* **5**, 1132–1139 (2005).
23. S. Sayil, D. V. Kerns, S. E. Kerns, Comparison of contactless measurement and testing techniques to a new all-silicon optical test and characterization method. *Ieee T. Instrum. Meas.* **54**, 2082–2089 (2005).
24. B. Legrand, Y. Dordet, J. Y. Voyant, J. P. Yonnet, Contactless position sensor using magnetic saturation. *Sensor. Actuat. A Phys.* **106**, 149–154 (2003).
25. P. P. Smith, K. Zografos, Sonar for recognising the texture of pathways. *Robot. Auton. Syst.* **51**, 17–28 (2005).
26. M. Gasulla, X. J. Li, G. C. M. Meijer, L. van der Ham, J. W. Spronck, A contactless capacitive angular-position sensor. *Ieee Sens. J.* **3**, 607–614 (2003).
27. Z. L. Wang, Triboelectric nanogenerators as new energy technology for self-powered systems and as active mechanical and chemical sensors. *ACS Nano* **7**, 9533–9557 (2013).
28. K. Y. Meng, J. Chen, X. S. Li, Y. F. Wu, W. J. Fan, Z. H. Zhou, Q. He, X. Wang, X. Fan, Y. X. Zhang, J. Yang, Z. L. Wang, Flexible weaving constructed self-powered pressure sensor enabling continuous diagnosis of cardiovascular disease and measurement of cuffless blood pressure. *Adv. Funct. Mater.* **29**, 1806388 (2019).
29. L. M. Zhao, H. Li, J. P. Meng, A. C. Wang, P. C. Tan, Y. Zou, Z. Q. Yuan, J. F. Lu, C. F. Pan, Y. B. Fan, Y. M. Zhang, Y. Zhang, Z. L. Wang, Z. Li, Reversible conversion between schottky and ohmic contacts for highly sensitive, multifunctional biosensors. *Adv. Funct. Mater.* **30**, 1907999 (2020).
30. Y. Ma, Q. Zheng, Y. Liu, B. J. Shi, X. Xue, W. P. Ji, Z. Liu, Y. M. Jin, Y. Zou, Z. An, W. Zhang, X. X. Wang, W. Jiang, Z. Y. Xu, Z. L. Wang, Z. Li, H. Zhang, Self-powered, one-stop, and multifunctional implantable triboelectric active sensor for real-time biomedical monitoring. *Nano Lett.* **16**, 6042–6051 (2016).
31. B. J. Shi, Z. Li, Y. B. Fan, Implantable energy-harvesting devices. *Adv. Mater.* **30**, 1801511 (2018).
32. J. Y. Sun, A. P. Yang, C. C. Zhao, F. Liu, Z. Li, Recent progress of nanogenerators acting as biomedical sensors in vivo. *Sci. Bull.* **64**, 1336–1347 (2019).
33. X. Chen, L. X. Gao, J. F. Chen, S. Lu, H. Zhou, T. T. Wang, A. B. Wang, Z. F. Zhang, S. F. Guo, X. J. Mu, Z. L. Wang, Y. Yang, A chaotic pendulum triboelectric-electromagnetic hybridized nanogenerator for wave energy scavenging and self-powered wireless sensing system. *Nano Energy* **69**, 104440 (2020).
34. X. Y. Li, J. Tao, X. D. Wang, J. Zhu, C. F. Pan, Z. L. Wang, Networks of high performance triboelectric nanogenerators based on liquid-solid interface contact electrification for harvesting low-frequency blue energy. *Adv. Energy Mater.* **8**, 1800705 (2018).
35. Y. C. Lai, J. N. Deng, S. M. Niu, W. B. Peng, C. S. Wu, R. Y. Liu, Z. Wen, Z. L. Wang, Electric eel-skin-inspired mechanically durable and super-stretchable nanogenerator for deformable power source and fully autonomous conformable electronic-skin applications. *Adv. Mater.* **28**, 10024–10032 (2016).
36. H. Ouyang, Z. Liu, N. Li, B. J. Shi, Y. Zou, F. Xie, Y. Ma, Z. Li, H. Li, Q. Zheng, X. C. Qu, Y. B. Fan, Z. L. Wang, H. Zhang, Z. Li, Symbiotic cardiac pacemaker. *Nat. Commun.* **10**, 1821 (2019).
37. Q. Zheng, Q. Z. Tang, Z. L. Wang, Z. Li, Self-powered cardiovascular electronic devices and systems. *Nat. Rev. Cardiol.* **18**, 7–21 (2021).
38. X. Qu, X. Ma, B. Shi, H. Li, L. Zheng, C. Wang, Z. Liu, Y. Fan, X. Chen, Z. Li, Z. L. Wang, Refreshable braille display system based on triboelectric nanogenerator and dielectric elastomer. *Adv. Funct. Mater.* **31**, 2006612 (2020).
39. G. Yao, L. Kang, C. Li, S. Chen, Q. Wang, J. Yang, Y. Long, J. Li, K. Zhao, W. Xu, W. Cai, Y. Lin, X. Wang, A self-powered implantable and bioresorbable electrostimulation device for

- biofeedback bone fracture healing. *Proc. Natl. Acad. Sci. U.S.A.* **118**, e2100772118 (2021).
40. H. Zou, Y. Zhang, L. Guo, P. Wang, X. He, G. Dai, H. Zheng, C. Chen, A. C. Wang, C. Xu, Z. L. Wang, Quantifying the triboelectric series. *Nat. Commun.* **10**, 1427 (2019).
 41. R. Hinchet, H. J. Yoon, H. Ryu, M. K. Kim, E. K. Choi, D. S. Kim, S. W. Kim, Transcutaneous ultrasound energy harvesting using capacitive triboelectric technology. *Science* **365**, 491–494 (2019).
 42. H. Guo, X. Pu, J. Chen, Y. Meng, M. H. Yeh, G. Liu, Q. Tang, B. Chen, D. Liu, S. Qi, C. Wu, C. Hu, J. Wang, Z. L. Wang, A highly sensitive, self-powered triboelectric auditory sensor for social robotics and hearing aids. *Sci. Robot.* **3**, eaat2516 (2018).
 43. F. Wen, Z. Sun, T. He, Q. Shi, M. Zhu, Z. Zhang, L. Li, T. Zhang, C. Lee, Machine learning glove using self-powered conductive superhydrophobic triboelectric textile for gesture recognition in VR/AR applications. *Adv. Sci.* **7**, 2000261 (2020).
 44. M. Zhu, T. He, C. Lee, Technologies toward next generation human machine interfaces: From machine learning enhanced tactile sensing to neuromorphic sensory systems. *Appl. Phys. Rev.* **7**, 031315 (2020).
 45. Y. H. Jung, S. K. Hong, H. S. Wang, J. H. Han, T. X. Pham, H. Park, J. Kim, S. Kang, C. D. Yoo, K. J. Lee, Flexible piezoelectric acoustic sensors and machine learning for speech processing. *Adv. Mater.* **32**, e1904020 (2020).
 46. H. S. Wang, T. H. Im, Y. B. Kim, S. H. Sung, S. Min, S. H. Park, H. E. Lee, C. K. Jeong, J. H. Park, K. J. Lee, Flash-welded ultraflat silver nanowire network for flexible organic light-emitting diode and triboelectric tactile sensor. *APL Mater.* **9**, e061112 (2021).
 47. M. Zhu, Z. Sun, T. Chen, C. Lee, Low cost exoskeleton manipulator using bidirectional triboelectric sensors enhanced multiple degree of freedom sensory system. *Nat. Commun.* **12**, 2692 (2021).
 48. C. Xu, Y. Zi, A. C. Wang, H. Zou, Y. Dai, X. He, P. Wang, Y.-C. Wang, P. Feng, D. Li, Z. L. Wang, On the electron-transfer mechanism in the contact-electrification effect. *Adv. Mater.* **30**, e1706790 (2018).
 49. Z. L. Wang, From contact electrification to triboelectric nanogenerators. *Rep. Prog. Phys.* **84**, 096502 (2021).
 50. Z. Zhou, K. Chen, X. Li, S. Zhang, Y. Wu, Y. Zhou, K. Meng, C. Sun, Q. He, W. Fan, E. Fan, Z. Lin, X. Tan, W. Deng, J. Yang, J. Chen, Sign-to-speech translation using machine-learning-assisted stretchable sensor arrays. *Nat. Electron.* **3**, 571–578 (2020).
 51. K. Englehart, B. Hudgins, A robust, real-time control scheme for multifunction myoelectric control. *Ieee T. Bio-med. Eng.* **50**, 848–854 (2003).

Acknowledgments

Funding: This work was supported by the National Key Research and Development Program of China (2021YFB3201200), Beijing Natural Science Foundation (JQ20038), Beijing Natural Science Foundation (L212010), the National Natural Science Foundation of China (T2125003), the National Natural Science Foundation of China (2102231), the National Natural Science Foundation of China (61875015), the National Natural Science Foundation of China (51902344), the National Natural Science Foundation of China (81971770), China Postdoctoral Science Foundation (2020M680302), and China Postdoctoral Science Foundation (2021T140041).

Author contributions: Conceptualization: Z. Li and X.Q. Methodology: Z. Li, D.L., and Z.L.W. Software: P.T. Investigation: X.Q., Z. Liu, C.W., and Y.L. Visualization: X.Q., P.T., H.F., and D.L. Funding acquisition: Z. Li, D.L., and Z. Liu. Project administration: Z. Li. Supervision: Z. Li. Writing—original draft: X.Q. and Z. Liu. Writing—review and editing: Z. Li and D.L.

Competing interests: The authors declare that they have no competing interests. **Data and materials availability:** All data needed to evaluate the conclusions in the paper are present in the paper and/or the Supplementary Materials.

Submitted 28 March 2022

Accepted 21 June 2022

Published 5 August 2022

10.1126/sciadv.abq2521